Optics Letters

Event-driven neuromorphic holography for dynamic particle imaging

ZHOU GE,[1,2] CHUTIAN WANG,[2] JIANQING HUANG,[2] AND EDMUND Y. LAM[2,*]

[1]School of Mechatronic Engineering and Automation, Shanghai University, Shanghai 200444, China
[2]Department of Electrical and Electronic Engineering, The University of Hong Kong, Hong Kong SAR, China
*elam@eee.hku.hk

Received 14 November 2024; revised 27 January 2025; accepted 27 January 2025; posted 29 January 2025; published 19 February 2025

Digital holography has emerged as a powerful tool for investigating dynamic particle behaviors in the spatiotemporal domain. However, the performance of this technique is fundamentally limited by the system's space–time bandwidth, leading to a trade-off between accuracy and speed. This study presents a novel, to the best of our knowledge, approach integrating event-driven neuromorphic imaging with digital holography for dynamic particle imaging. Through comprehensive analysis of synthetic and real-world experiments, we demonstrate that the proposed method significantly improves data efficiency and hologram contrast by over tenfold. This technique, termed "neuromorphic holography," offers promising applications for efficient dynamic particle imaging.

https://doi.org/10.1364/OL.548088

The study of dynamic particle behaviors holds significant importance across various research fields, including fluid mechanics, cellular analysis, and pollution assessment [1–3]. Numerous optical techniques have been proposed for dynamic particle imaging, including tomographic imaging [4], laser Doppler [5], and digital holography [6]. Among these, digital holography has emerged as a prominent approach due to its inherent advantages of full-field imaging, refocusing capability, and label-free operation [7]. Inline and off-axis configurations are commonly employed for digital holographic particle imaging, with the off-axis setup providing a narrower depth of focus by separating the twin and DC terms during reconstruction. Nevertheless, the inline configuration remains appealing due to its simple optical setup and higher light efficiency [8].

Dynamic holographic particle imaging operates by exploiting the interference between the reference beam and the scattered light from particles within the same optical path [9]. The interference patterns of dynamic particles are recorded as a sequence of holograms using a digital imager, such as a charge-coupled device (CCD). Each frame in the hologram sequence undergoes repeated numerical reconstruction or fringe analysis, facilitating the extraction of spatiotemporal information regarding the particle's position, velocity, and morphology [10]. Despite decades of advancement, dynamic holographic particle imaging still encounters several limitations. One prominent issue is the low contrast of holograms, due to background distortions and illumination artifacts. Consequently, pre-processing of raw holograms is essential for accurate particle imaging but at the expense of higher operational complexity. Another constraint is the low data efficiency inherent to the frame-based imaging scheme in video-rate digital holography, where continuous particle behaviors are recorded as a sequence of static holograms. As a result, temporal information is limited by the sampling rate, and kinematic features can only be inferred through the complex motion recovery algorithm [11]. Various methods have been proposed to address these challenges including high-speed imaging [12], compressive sensing [13,14], and streak velocimetry [15]. However, these approaches often lead to excessive oversampling and large data volumes, imposing substantial burdens on subsequent data processing and analysis.

Inspired by the efficient processing mechanism of the human vision system, bio-inspired neuromorphic imaging has emerged as a powerful technique for dynamic imaging, leveraging event-driven sparse coding and neural adaptation [16,17]. Unlike traditional imaging methods, which capture and analyze absolute intensities across the entire field of view, neuromorphic imaging asynchronously detects and responds to changes in light intensity at the per-pixel level, represented as neural spikes or events. This bio-inspired approach offers several distinct advantages, including high temporal precision, wide dynamic range, and low data redundancy. Neuromorphic imaging has driven advancements in various imaging fields including speckle imaging [18,19], wavefront sensing [20,21], optical encryption [22], bispectral photometry [23], and autofocusing [24,25].

In this Letter, we introduce a novel event-driven neuromorphic methodology to overcome the limitations encountered in dynamic holographic particle imaging. Our approach captures changes in light intensity within holographic recordings as neural spikes, enabling particle depth determination through neuromorphic fringe analysis. Both synthetic and real-world experiments were conducted to validate the effectiveness of our proposed approach. The results demonstrate a significant enhancement in data efficiency and hologram contrast by over tenfold. This innovative approach, termed "neuromorphic holography," not only contributes to the advancement of particle-related investigations but also establishes a promising direction for the future development of digital holography.

In an inline holographic particle imaging system, a coherent plane wave is employed to illuminate a particle volume, shown

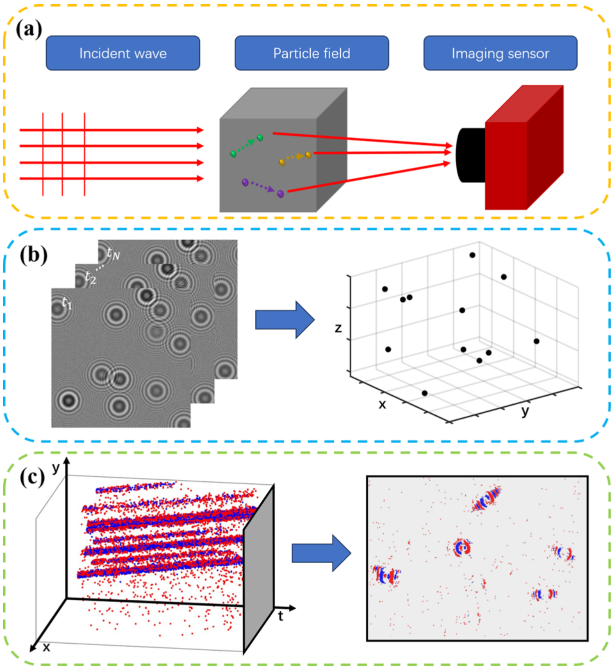

Fig. 1. Schematic of dynamic holographic particle imaging. (a) A plane wave is incident on a particle field, and holograms are recorded by an imaging sensor. (b) Particle locations are determined by analyzing the digital holograms. (c) Spatiotemporal variations in the scattered field are recorded as sparse neural spikes, forming neuromorphic holograms through the accumulation of event polarity.

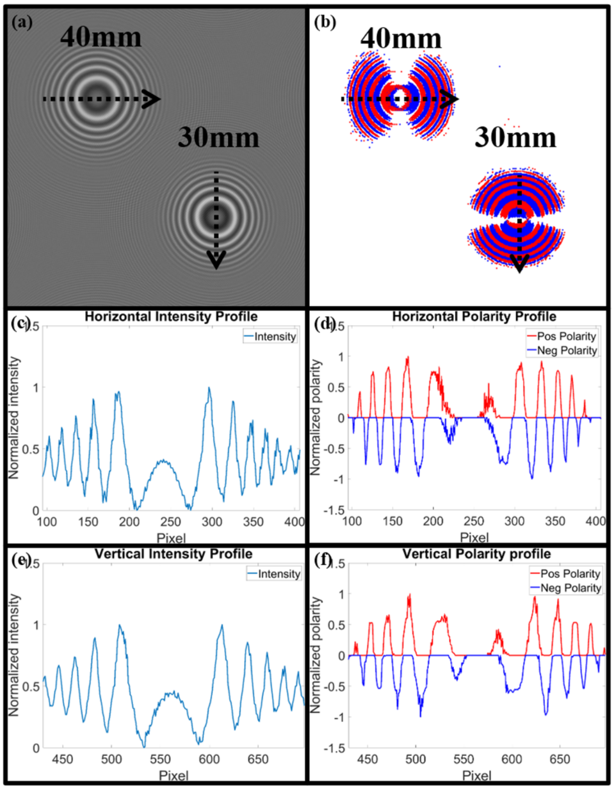

Fig. 2. Comparative simulation results. (a), (b) Digital and neuromorphic holograms of sphere particles with different depths and motion directions. (c), (d) Cross-sectional profiles of the horizontally translating particle. (e), (f) Cross-sectional profiles of the vertically translating particle.

in Fig. 1(a). The captured hologram can be formulated as follows [26]:

$$I(\mathbf{r}) = \left|E_0(z - z_p) + E_s(r - r_p)\right|^2, \tag{1}$$

where $E_0(z - z_p)$ is the incident plane wave propagating along the z axis, with the particle located at the axial position z_p, and $E_s(r - r_p)$ is the scattered wave that propagates from the particle at r_p to the point of observation r. As shown in Fig. 1(b), each particle's location in the 3D space can be determined through texture analysis or numerical reconstruction. However, obtaining spatiotemporal information requires capturing and processing multiple holograms sequentially, which increases both data volume and computational cost.

Unlike the frame-based holographic imaging method that acquires redundant frame stacks, the proposed event-driven dynamic holographic particle imaging approach captures light changes as sparse neural spikes and forms neuromorphic holograms through event polarity accumulation, as illustrated in Fig. 1(c). According to the linearized event generation model [27], an event $e_k \doteq (\mathbf{x}_k, t_k, p_k)$ conveys that the logarithmic brightness L at pixel $\mathbf{x}_k$ changes by a predefined contrast threshold C. This relationship can be formulated as follows:

$$\Delta L(\mathbf{x}_k, t_k) = L(\mathbf{x}_k, t_k) - L(\mathbf{x}_k, t_k - \Delta t_k) = p_k C, \tag{2}$$

where polarity $p_k \in \{+1, -1\}$ is the sign of the brightness change and Δt_k is the time since the last event at pixel $\mathbf{x}_k$. Given a set of events $\mathcal{E} = \{e_k\}_{k=1}^{N_e}$, accumulating their polarities in a pixel-wise manner produces a brightness increment image $B(\mathbf{x})$ given by the following:

$$B(\mathbf{x}) = \sum_{t_k \in \Delta t} p_k C \delta(\mathbf{x} - \mathbf{x}_k), \tag{3}$$

where δ is the Kronecker delta function selecting the pixel $\mathbf{x}_k$. Assuming Δt is small enough, brightness increments are evoked only by the brightness gradients ΔL (see Supplement 1 for a detailed derivation). As a result, Eq. (3) can be approximated as follows:

$$B(\mathbf{x}) = \Delta L(\mathbf{x}) \approx -\nabla L(\mathbf{x}) \cdot \Delta \mathbf{x}. \tag{4}$$

The proposed approach achieves efficient dynamic holographic particle imaging by integrating event-driven neuromorphic imaging with digital holography. The brightness increment image, $B(\mathbf{x})$, efficiently encodes particles' spatiotemporal information. Decoding is accomplished through fringe analysis based on hologram texture correlation, as outlined in [28]. To provide quantitative comparisons for the improvement in holographic imaging, we utilized two evaluation metrics: data efficiency and image contrast. Data efficiency is calculated as the ratio of pixels occupied by the interference pattern to the total frame size. Image contrast is calculated as the root mean square (RMS) of the hologram intensity/polarity values.

Comparative simulations were conducted to demonstrate the effectiveness of the proposed method in dynamic holographic particle imaging. In these simulations, two particles of identical diameter 60 µm were positioned at different depths and translated in different directions. A sequence of digital holograms, with a resolution of 800×800 and a pixel size of 5 µm, was generated using the Fresnel diffraction, as illustrated in Fig. 2(a). The particle in the upper left was located 40 mm from the imaging plane and moved horizontally, while the particle in the bottom right was positioned 30 mm from the imaging plane and moved vertically. In the Fresnel diffraction of uniformly sized circular particles, differences in propagation distances affect the wavefront phase and spatial distribution, resulting in distinct diffraction patterns on the imaging plane. The radius of these diffraction rings can be estimated as $r_n = \sqrt{n\lambda z}$, where n is the order number, λ is the wavelength, and z is the propagation distance. Consequently, particles located farther from the imaging plane generate smoother and more diffused patterns as the propagation distance increases, enabling 3D localization through 2D texture analysis of the holograms. However, since moving particles and the stationary background are recorded together in the image, extracting temporal information—such as particle motion direction—from a single hologram remains challenging.

Neuromorphic holograms were simulated through event polarity accumulation from the sequence of digital holograms using the video-to-event (v2e) simulator [29]. The resulting neuromorphic hologram is presented in Fig. 2(b) where red and blue dots denote positive and negative polarities of contrast changes in the scattered field, respectively. In contrast to digital holograms that display uniform diffraction patterns, neuromorphic holograms exhibit distinct features associated with particle motion. Notably, neuromorphic holograms display alternating polarity patterns that correspond to the bright and dark rings of diffraction patterns. For instance, the first-order bright diffraction ring generates positive events in the direction of motion and negative events in the opposite direction, creating an inner diffraction ring with contrasting polarities. Additionally, neuromorphic holograms exhibit a pair of symmetrical event-free notches located on opposite sides along the motion direction. This phenomenon arises from the minimal contrast variations at particle edges aligned with the motion direction, which fall below the threshold C specified in Eq. (2). As a result, the neuromorphic holographic representation features a concentric pattern interspersed with two event-free notches. This unique attribute enables the characterization of particle motion from a snapshot neuromorphic hologram. Additional comparisons in particle overlapping and axial displacement can also be found in Figs. S1 and S2 of Supplement 1.

The proposed dynamic holographic particle imaging approach was evaluated through both qualitative and quantitative analyses. The cross-sectional profiles of the dynamic particles along their motion directions in both the digital and neuromorphic holograms are shown in Figs. 2(c)–2(f). These profiles reveal oscillatory peak-and-valley patterns, resulting from alternating constructive and destructive interference in the holograms. In the digital hologram, the horizontally translating particle at a propagation distance of 40 mm shows six orders of diffraction rings, with the radius of the first-order ring measuring approximately 62 pixels. Similarly, in the neuromorphic hologram, six orders of diffraction rings are observed, with the first-order ring radius approximately 61 pixels. For the vertically translating particle at a propagation distance of 30 mm, five orders of diffraction rings are present in both the digital and neuromorphic holograms, with the first-order ring radius about 56 pixels. The simulation results align closely with the diffraction theory, demonstrating the effectiveness of the proposed event-driven approach. Due to the motion-specific nature of neuromorphic imaging, low-frequency features such as static background and zeroth-order maxima do not trigger events in the neuromorphic holograms. In the full 800×800 frame, only 39,906 pixels are activated in the neuromorphic hologram shown in Fig. 2(b), representing 6.2% data efficiency.

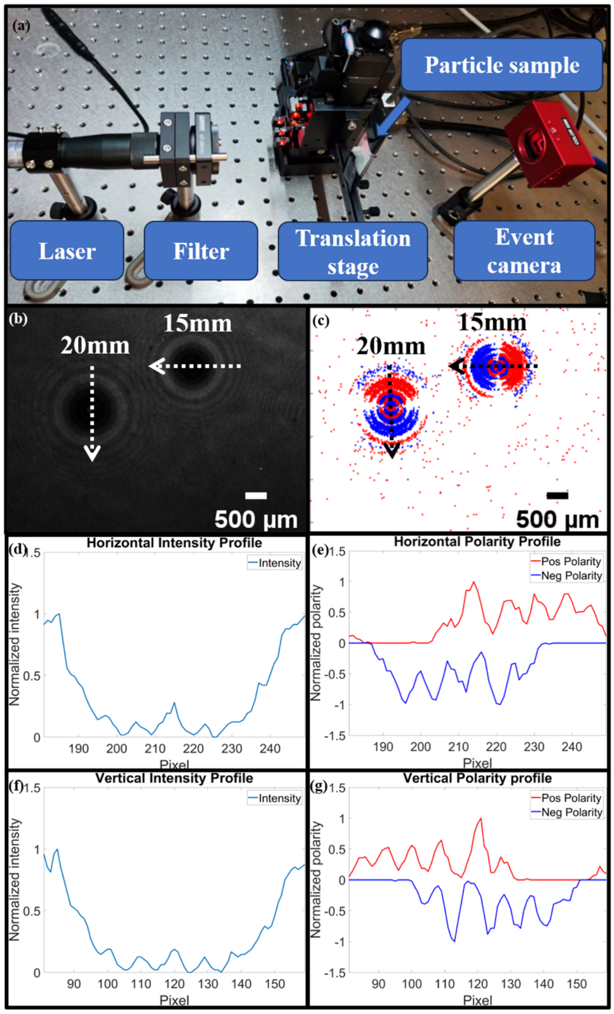

Fig. 3. Experimental setup and results. (a) Overview of the inline holographic imaging setup. (b), (c) Digital and neuromorphic holograms of dynamic particles with different depths and moving directions (Visualization 1 and Visualization 2). (d), (e) Cross-sectional profiles of the horizontally translating particle. (f), (g) Cross-sectional profiles of the vertically translating particle.

The image contrast for the digital hologram and neuromorphic hologram is 0.13 and 3.99, respectively. Consequently, the proposed technique offers significant improvement in data efficiency and image contrast, reducing storage requirements and enhancing accuracy.

Then, a proof-of-concept dynamic holographic particle imaging experiment was conducted to validate the effectiveness of the proposed method in practical applications. As shown in Fig. 3(a), a collimated laser source (100 mW, 650 nm, FU650AD100, Fulaser) with a bandpass filter (CWL = 650 nm, FBH650-3, Thorlabs) was directed onto particles placed on microscope slides and manipulated by motorized translation stages (WN262TA20, Winner Optics). The interference patterns were recorded using a neuromorphic event camera (346×260 resolution, 18.5 µm pixel size, DAVIS 346, iniVation) as both neuromorphic events and traditional frames. The recorded events are aggregated into neuromorphic holograms with 50 ms accumulation time, the same as the exposure time for digital holograms. In the experiment, polystyrene microspheres with a diameter of 1 mm served as test particles. They were positioned at two distinct planes from the imaging sensor and controlled to move in varying directions to emulate dynamic particles in the 3D space.

The captured digital hologram is shown in Fig. 3(b) with annotated particle depth and motion direction. In practical applications, system parameters such as light source power and camera exposure settings significantly affect signal-to-noise ratio (SNR), which in turn impacts particle imaging quality. In the raw digital hologram without any pre-processing, the fringes exhibit low contrast and the number of orders and diffraction ring radius is difficult to distinguish. In contrast, as shown in Fig. 3(c), the neuromorphic hologram, taken under the same conditions, exhibits rich textural information with very few background events, indicating a high SNR. Only 5459 pixels are activated in the neuromorphic hologram, accounting for 6.1% of the frame size. The image contrast for the digital and neuromorphic holograms is 0.36 and 4.85, respectively. The neuromorphic method significantly improves data efficiency and hologram contrast by over tenfold. Furthermore, the unique shape of the polarities indicates the motion direction, which is not identifiable from a single digital hologram.

The cross-sectional profiles of the dynamic particles along their motion directions in the digital and neuromorphic holograms are presented in Figs. 3(d)–3(g). Due to limited dynamic range and background noise, the interference pattern in the digital hologram exhibits relatively low variation. In contrast, the neuromorphic representation clearly reveals oscillatory peak-and-valley patterns, demarcating diffraction ring orders. In the digital hologram, two orders of diffraction rings can be recognized for both particles at different depths, with the radius of the first-order ring measuring approximately 11 pixels for the horizontally translating particle at a propagation distance of 15 mm and 9 pixels for the vertically translating particle at a propagation distance of 20 mm. In the neuromorphic hologram, five orders of diffraction rings can be recognized for the horizontally translating particle at a shorter propagation distance, and six orders of diffraction rings are discernible for the vertically translating particle at a longer propagation distance. The radius of the first-order ring measures 9 pixels for the horizontally translating particle and 12 pixels for the vertically translating particle. These results indicate that the proposed neuromorphic holography achieves accurate measurements for dynamic particles, whereas traditional digital holography proves inadequate.

In conclusion, we propose an event-driven neuromorphic holography approach for dynamic particle imaging. By leveraging the neuromorphic imaging technique, spatiotemporal information can be effectively obtained from a single hologram. Compared with conventional digital holographic imaging methods, both synthetic and real-world experiments demonstrate over a tenfold improvement in data efficiency and image contrast. This innovative approach, termed "neuromorphic holography," opens new avenues for future research and establishes a promising direction for advancing digital holography.

Funding. University Grants Committee (GRF 17201620); Shanghai University (SUITM-202415).

Disclosures. The authors declare no conflicts of interest.

Data availability. Data underlying the results presented in this Letter are not publicly available at this time but may be obtained from the authors upon reasonable request.

Supplemental document. See Supplement 1 for supporting content.

REFERENCES

1. D. Pirone, D. Sirico, L. Miccio, *et al.*, Lab Chip **22**, 793 (2022).
2. J. Huang, S. Li, W. Cai, *et al.*, Combust. Flame **230**, 111430 (2021).
3. J. Huang, Y. Zhu, Y. Li, *et al.*, ACS Photonics **10**, 4483 (2023).
4. F. García-Moreno, P. H. Kamm, T. R. Neu, *et al.*, Adv. Mater. **33**, 2104659 (2021).
5. R. Sijs, S. Kooij, H. Holterman, *et al.*, AIP Adv. **11**, 015315 (2021).
6. Y. Zhang, Y. Zhu, and E. Y. Lam, Appl. Opt. **61**, B111 (2022).
7. J. Zhang, J. Sun, Q. Chen, *et al.*, IEEE Trans. Comput. Imaging **6**, 697 (2020).
8. T. Zeng, Y. Zhu, and E. Y. Lam, Opt. Express **29**, 40572 (2021).
9. T.-H. Chao and H.-K. Liu, Appl. Opt. **28**, 226 (1989).
10. E. Çetintaş, Y. Luo, C. Nguyen, *et al.*, Sci. Rep. **12**, 3175 (2022).
11. M. Rogalski, J. A. Picazo-Bueno, J. Winnik, *et al.*, Sci. Rep. **12**, 12909 (2022).
12. Y. Wu, Q. Wang, and C. Zhao, Meas. Sci. Technol. **32**, 065011 (2021).
13. Y. Gao and L. Cao, Optica **11**, 32 (2024).
14. P. W. Tsang, J.-P. Liu, and T.-C. Poon, Optica **2**, 476 (2015).
15. L. Dixon, F. C. Cheong, and D. G. Grier, Opt. Express **19**, 4393 (2011).
16. P. Zhang, H. Liu, Z. Ge, *et al.*, IEEE Trans. on Image Process. **33**, 2318 (2024).
17. P. Zhang, Z. Ge, L. Song, *et al.*, IEEE Trans. Comput. Imaging **9**, 530 (2023).
18. Z. Ge, Y. Gao, H. K.-H. So, *et al.*, Opt. Lett. **46**, 3885 (2021).
19. Z. Ge, P. Zhang, Y. Gao, *et al.*, Opt. Express **30**, 2206 (2022).
20. C. Wang, S. Zhu, P. Zhang, *et al.*, Laser Photonics Rev. **1**, 2400647 (2024).
21. F. Kong, A. Lambert, D. Joubert, *et al.*, Opt. Express **28**, 36159 (2020).
22. S. Zhu, C. Wang, J. Huang, *et al.*, Adv. Photon. Nexus **3**, 056002 (2024).
23. T. Takatani, Y. Ito, A. Ebisu, *et al.*, in *Proceedings of the IEEE/CVF Conference on Computer Vision and Pattern Recognition* (2021), pp. 15638–15647.
24. X. Qu, C. Ma, W. Hu, *et al.*, Opt. Lasers Eng. **175**, 108025 (2024).
25. Z. Ge, H. Wei, F. Xu, *et al.*, Opt. Lasers Eng. **160**, 107247 (2023).
26. F. C. Cheong, B. S. Rémi Dreyfus, J. Amato-Grill, *et al.*, Opt. Express **17**, 13071 (2009).
27. D. Gehrig, H. Rebecq, G. Gallego, *et al.*, Int. J. Comput. Vis. **128**, 601 (2020).
28. S. Seo, T.-W. Su, D. K. Tseng, *et al.*, Lab Chip **9**, 777 (2009).
29. Y. Hu, S.-C. Liu, and T. Delbruck, in *Proceedings of the IEEE/CVF Conference on Computer Vision and Pattern Recognition* (2021), pp. 1312–1321.